Optically Tunable Mesoscale CdSe Morphologies Via Inorganic Phototropic Growth†

Kathryn R. Hamann,‡[a] Azhar I. Carim,‡[a] Madeline C. Meier,[a] Jonathan R. Thompson,[b] Nicolas A. Batara,[b] Ivan S. Yermolenko,[c] Harry A. Atwater[b] and Nathan S. Lewis*[a]

[a] *Division of Chemistry and Chemical Engineering, California Institute of Technology, Pasadena, CA 91125, USA. E-mail: nslewis@caltech.edu*

[b] *Division of Engineering and Applied Sciences, California Institute of Technology, Pasadena, CA 91125, USA*

[c] *Bruker Corporation, Nano Surfaces Division, San Jose, CA 95134, USA*

† Electronic supplementary information (ESI) available.

‡ These authors contributed equally (KRH and AIC)

Inorganic phototropic growth using only spatially conformal illumination generated Se-Cd films that exhibited precise light-defined mesoscale morphologies including highly ordered, anisotropic, and periodic ridge and trench nanotextures over entire macroscopic substrates. Growth was accomplished via a light-induced electrochemical method using an optically and chemically isotropic solution, an unpatterned substrate, and unstructured, incoherent, low-intensity illumination in the absence of chemical directing agents or physical templates and masks. The morphologies were defined by the illumination inputs: the nanotexture long axes aligned parallel to the optical E-field vector, and the feature sizes and periods scaled with the wavelength. Optically based modeling of the growth closely reproduced the experimental results, confirming the film morphologies were fully determined by the light-matter interactions during growth. Solution processing of the Se-Cd films resulted in stoichiometric, crystalline CdSe films that also exhibited ordered nanotextures, demonstrating that inorganic phototropic growth can effect tunable, template-free generation of ordered CdSe nanostructures over macroscopic length scales.

Introduction

Nature spontaneously generates ordered mesostructured interfaces that exhibit unique optical and mechanical properties beneficial to biological fitness.[1, 2] Artificial mimics of structured biological surfaces are of interest for numerous applications including improving light-trapping in photovoltaic applications, constructing microfluidic systems, and developing anti-fouling and anti-corrosion coatings.[3-5] Mesostructured interfaces can be generated in artificial systems using illumination with an anisotropic spatial intensity profile to effect confinement of photo-driven chemical reactions. Spatially structured illumination can be generated by filtering a conformal light source through a photomask, by diffraction through a grating, or by beam rastering. Such structured illumination can initiate spatially selective polymerization, decomposition or cross-linking in an organic precursor film to produce an interface that exhibits spatially non-homogenous chemistry.[6] Confined illumination at a solid surface can isolate physical ablation as well as chemical deposition and etching in the presence of vapor-phase reagents.[7, 8] Spatially selective illumination can also effect localized charge-carrier generation in solution-immersed semiconductor substrates, leading to confined electrochemical deposition or etching.[9-12]

Alternatively, unstructured, isotropic illumination fields can generate mesoscale morphologies by exploiting inherent asymmetries in the interactions of light with matter.[13, 14] Such approaches enable direction of morphological outcomes on the nanoscale and mesoscale, and enable structuring below the optical diffraction limit, by manipulation of the attributes of the optical excitation beyond the far-field spatial intensity profile.[15, 16] Photo-driven, plasmon-mediated growth of surficial Ag nanoparticles can yield arrays having a uniform particle size that is a function of the optical wavelength and anisotropic particle shape orientation related to the direction of optical polarization.[17] Light-induced isomerization, and subsequent mechanical

motion of molecules in organic films in close proximity to metal nanoparticles, can also yield sub-wavelength surface topographies that are specified by the input wavelength and polarization state.[18, 19]

Biological systems can exhibit directed and/or structured growth in response to unstructured, isotropic illumination fields via a process called phototropism, wherein growth is effected by a positive-feedback mechanism that optimizes solar energy harvesting.[20-23] For example, spatially directed phototropic growth produces the observed mesoscale morphologies of palm trees and foliaceous coral.[22, 23] Recently, analogous inorganic phototropic growth of chalcogen alloys has been observed wherein the mesoscale morphologies of photoelectrochemically generated films are defined by the optical characteristics of the illumination used to drive growth.[24-27] Such inorganic phototropic growth occurs due to preferential addition of mass in areas of spontaneous local optical field intensity elevation during growth, and provides optical control over the film morphology at the mesoscale without structured illumination fields nor chemical or physical anisotropy in the solution or substrate.

In this work, we demonstrate that mesostructured morphologies of an important semiconductor material, CdSe, can be generated and controlled via inorganic phototropic growth. CdSe is a direct bandgap semiconductor with an absorption edge in the visible region of the electromagnetic spectrum. Substantial effort has been directed towards controlling the crystal habit and morphology of colloidally synthesized CdSe nanocrystals via the use of chemical directing agents.[28-30] Mesostructured CdSe films have been fabricated by numerous methods on solid substrates using solution-grown nanoparticles, including the use of ligand-directed assembly, infilling of solid supports, and polymer encapsulation.[31-33] Structured CdSe films have also been generated via electrochemical deposition into physical templates.[34, 35] CdSe films generated via

both colloidal and electrochemical routes are being studied extensively for many applications including use as photodetectors, solar light absorbers, and light-emitters.[36-41] Herein, inorganic phototropic growth was used to generate mesostructured Se-Cd films. Growth was performed using spatially conformal illumination with varying input wavelengths and polarizations, and the morphological outcomes were assessed as a function of the characteristics of the optical inputs. The growth process was modeled using simulations of the optical processes at the growth interface, confirming the interactions that directed the mesoscale morphological evolution. The Se-Cd films were then processed via immersion in $CS_{2(l)}$, to produce stoichiometric, polycrystalline CdSe mesostructures over macroscopic areas (i.e. an entire electrode substrate).

Results and discussion

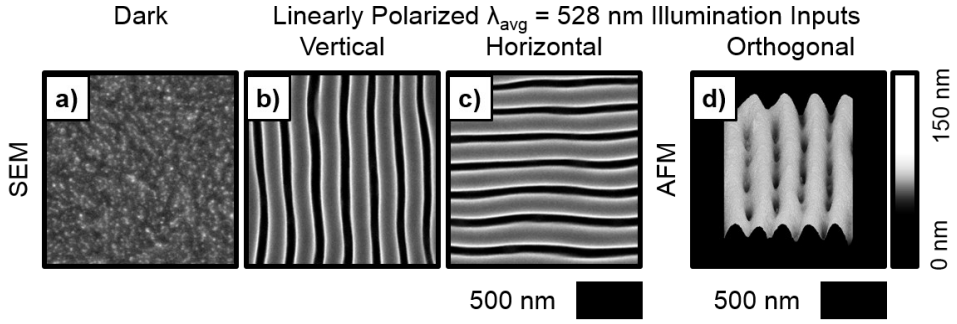

Figure 1. SEMs representative of films generated (a) in the dark and using (b) vertically polarized, and (c) horizontally polarized, λ_{avg} = 528 nm illumination. (d) Perspective-view AFM representative of a film generated by inorganic phototropic growth in a single step using two orthogonally polarized λ_{avg} = 528 nm illumination inputs (a 0.7 fraction of the total intensity was provided in one polarization and the balance in the orthogonal polarization).

Se-Cd films were electrochemically grown on a Au-coated n^+-Si substrate from an aqueous solution of 0.00500 M SeO_2, 0.200 M $CdSO_4$, and 0.100 M H_2SO_4 (additional experimental details in the Supplementary Information). Figure 1a presents a representative scanning-electron micrograph (SEM) of a film grown in the dark, showing a lack of ordered surface texture. In contrast, Figure 1b presents a representative SEM of a film grown under incoherent illumination from a light-emitting diode (LED) source with an intensity-weighted average wavelength, λ_{avg}, of 528 nm and polarized linearly with the E-field vector aligned along the vertical. No far-field spatial

manipulation of the light field was utilized, and the same intensity, wavelength, and linear polarization was delivered to each point of substrate, yet the film displayed a sharply defined, highly anisotropic, periodic ridge and trench nanotexture, with features oriented vertically and generated conformally over the entire surface of the macroscopic substrate (0.50 cm x 0.50 cm). Figure 1c presents a representative SEM of a film grown in a similar manner to that presented in Figure 1b but with the illumination polarized such that the E-field vector aligned horizontally, revealing a similar nanotexture but with horizontally oriented features. Figure 1d presents a representative atomic-force micrograph (AFM) of a film grown using simultaneous illumination from two orthogonally polarized λ_{avg} = 528 nm LED sources with non-equal intensities. The micrograph depicts the full three-dimensional topography, as well as cross-sectional profile, of the film produced under these illumination conditions. This intricate three-dimensional morphology exhibited an anisotropic, periodic ridge and trench nanotexture similar to that observed with a single polarized illumination input (Figure 1b and c), but with an additional shorter intersecting ridge and trench motif having features that were periodic in the direction orthogonal to the periodicity of the taller motif. The observation of two morphological components with orthogonal periodicities correlates with the use of two orthogonally polarized optical inputs during the single growth process step. These data highlight the potential of the inorganic phototropic growth technique, in single process step with only unstructured illumination and an unstructured substrate, to readily generated surfaces having the three-dimensional structure necessary to mimic those observed in purpose-evolved biological interfaces.[42, 43] Scaling of the process to generate such surfaces over large macroscale areas may be accomplished simply by use of illumination that conformally fills the target region. Inorganic phototropic growth does not require use of coherent nor monochromatic illumination: any incandescent, LED, or laser sources, as well as sunlight,

could provide light input at the requisite scale.[25] Additionally, chemical or physical exfoliation, e.g. by substrate dissolution using a selective etchant or polymer encapsulation followed by mechanical separation, could be used to remove the phototropically grown films from the conductive growth support to enable applications requiring freestanding structures or nonconductive substrates.[44, 45]

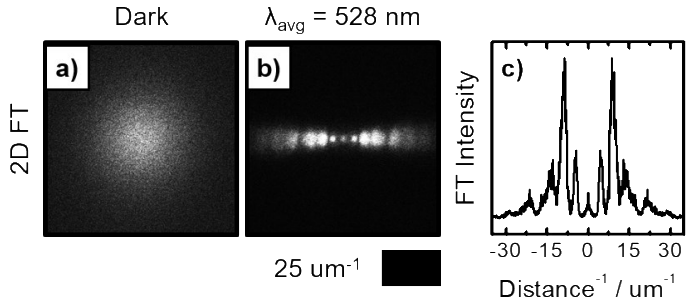

Figure 2. 2D FTs derived from SEMs of films generated (a) in the dark and using (b) vertically polarized λ_{avg} = 528 nm illumination. (c) Fourier spectrum derived from the 2D FT in (b).

Figures 2a and b present two-dimensional Fourier transforms (2D FTs) derived from SEM data for each of the films depicted in Figures 1a and b, respectively. Brightness in each 2D FT is indicative of the periodic components in the micrograph from which the 2D FT data were derived. The distance from the center is representative of the component frequency, and the direction relative to the center is the direction of periodicity. The film grown in the dark (Figure 1a) exhibited a broad and diffuse circular 2D FT profile (Figure 2a), consistent with the isotropic and unpatterned film morphology. The Se-Cd film grown using vertically polarized illumination (Figure 1b) exhibited a 2D FT profile characterized by a tight, narrow band of well-defined spots aligned along the horizontal (Figure 2b), consistent with the highly anisotropic and ordered nature of the phototropically grown film. These data indicate that the nanotexture periodicity was generated only in the direction perpendicular to the E-field vector of the illumination during growth. Figure 2c presents a Fourier spectrum obtained by integrating the grayscale intensity through the horizontal centerline of the 2D FT for the film grown using vertical polarization (Figure 2b). The

Fourier spectrum revealed a single family of related components consisting of a fundamental frequency along with several higher frequency overtones. The inverse of the fundamental frequency is equivalent to the period of the ridge and trench nanotexture (e.g. distance between identical points on two neighboring ridges). The morphological period was 214 ± 3 nm for films grown using linearly polarized λ_{avg} = 528 nm illumination. The presence of the overtones in the Fourier spectrum indicates that the topological profile of the surface texture in the films does not conform precisely to a sinusoidal profile. The substantial overtone intensity is consistent with the sharp in-plane morphological contrast of the surface texture, indicating that inorganic phototropic growth can effect substantial in-plane anisotropy in the absence of anisotropic or structured illumination inputs. Additionally, the sharp definition of both the fundamental and the associated overtones and the relatively low signal at zero frequency in the Fourier spectrum are consistent with the high mesoscale fidelity of the nanotextures, which exhibited a dislocation and disclination defect density of 0.04 per square morphological period, comparable to that observed in films of organic block copolymers with similar structural motifs generated via templateless self-assembly.[46, 47]

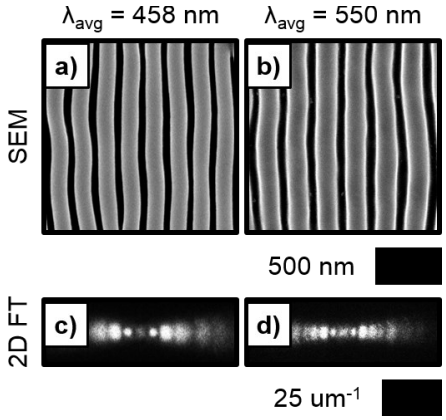

Figure 3. (a) and (b) SEMs representative of films generated by inorganic phototropic growth using vertically polarized illumination with the indicated λ_{avg}. (c) and (d) 2D FTs generated from SEMs of the films depicted in (a) and (b), respectively.

Figure 3a and b present representative SEMs of films generated by inorganic phototropic growth using vertically polarized LED sources with λ_{avg} = 458 and 550 nm, respectively. Use of either illumination source during growth effected nanotextures that exhibited vertically oriented, anisotropic features similar to those observed using vertically polarized λ_{avg} = 528 nm illumination (Figure 1b). The use of λ_{avg} = 458 nm illumination (Figure 3a) resulted in the generation of a smaller feature size and smaller apparent morphological period than when λ_{avg} = 528 nm (Figure 1b) was used, whereas use of λ_{avg} = 550 nm illumination (Figure 3b) resulted in a larger feature size and a larger apparent morphological period, indicating that both the feature size and period are controlled by the λ_{avg} of the illumination during inorganic phototropic film growth. Figure 3c and d present 2D FTs derived from SEM data of films generated with vertically polarized λ_{avg} = 458 and 550 nm illumination, respectively. Both sets of data were qualitatively similar to the 2D FT data derived from films produced by growth using λ_{avg} = 528 nm (Figure 2b). The spots in the 2D FTs for λ_{avg} = 458 and 550 nm (Figure 3c and d) were spaced further apart, and closer together, respectively, than for λ_{avg} = 528 nm (Figure 2b), consistent with the respective smaller and larger morphological periods apparent in the SEM data (Figure 3a and b) of those systems. Further analysis of the 2D FT data revealed only a single fundamental frequency and associated overtones in each case, suggesting that each value of λ_{avg} encodes for a singular period in the film morphology. Quantitatively, the Fourier analysis indicated periods of 184 ± 4 nm and 230 ± 3 nm for Se-Cd films generated using λ_{avg} = 458 and 550 nm, respectively.

The nanotextures produced by inorganic phototropic growth were hypothesized to be an emergent phenomenon that is a consequence of spatially varying deposition rates resulting from anisotropic coupling between the growing film and the incident illumination. Electromagnetic simulations of the growth process were therefore performed to validate this mechanism of

nanotexture formation. A two-step iterative model was used (full modeling details in the Supplementary Information) in which the spatially dependent photocarrier generation rates at the growth interface were first calculated using full-wave electromagnetic simulations. A Monte Carlo method was then used to simulate light-motivated electrochemical growth, with the probability of local mass addition weighted by the local photocarrier generation rate. Empirical inputs to the model were minimal and included estimates of the real and imaginary parts of the complex refractive index of the electrochemically grown material. The results of the model are thus principally defined by the light-matter interactions at the growth interface.

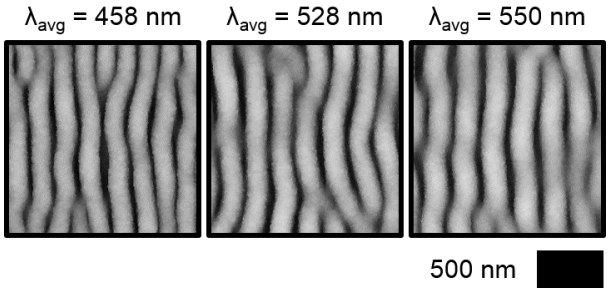

Figure 4. Simulated morphologies films generated by inorganic phototropic growth using vertically polarized illumination with the indicated λ_{avg}.

Figure 4 presents simulated morphologies for inorganic phototropic growth using vertically polarized illumination with λ_{avg} = 458, 528, and 550 nm. In each case, vertically oriented, periodic and anisotropic ridge and trench nanotextures were produced with spatial characteristics in close accord with the analogous experimental SEM data for such films (Figure 3a, Figure 1b, and Figure 3b). The characteristic morphological period of the films as determined by FT analysis was 195 ± 8 nm, 219 ± 10 nm, and 230 ± 11 nm for simulations using λ_{avg} = 458, 528, and 550 nm illumination, respectively, thus quantitatively agreeing with the experimental observations of Se-Cd film growth. This agreement, given the optical basis of the model, confirms that the film morphology is a function of the optical characteristics of the photoelectrochemically prepared material and also indicates that observed mesostructure development is primarily instructed by spatially-varying

photocarrier generation rather than photothermal and related physical phenomena. Additionally, the simulation data, given the limited empirical input parameters, along with the empirical results, suggests that inorganic phototropic growth is not uniquely demonstrable in the case of a singular, discrete material but rather may be observed in broad range of materials with suitable intrinsic optoelectronic properties.

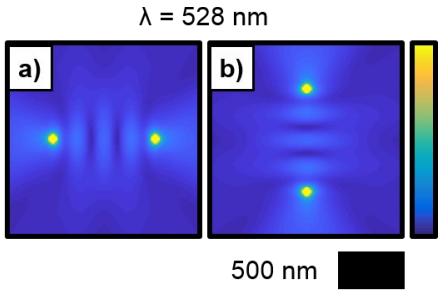

Figure 5. Normalized time-average of the E-field magnitude from two dipoles emitting radiation with a free space wavelength of λ = 528 nm in a medium of refractive index n = 1.33. Dipoles separated by a distance of twice the wavelength (a) along the horizontal and (b) along the vertical with the oscillation axis perpendicular to the axis of separation.

Additional simulations were performed to explore the fundamental optical interactions that underpin the nanotexture formation. Initial electrochemical growth results in the generation of surface asperities that can scatter input illumination. Dipole emission sources were utilized to model such asperities and the associated light scattering to investigate the interfacial modulation of the E-field during growth. Figure 5a presents a simulation of the normalized time-average of the E-field magnitude from two dipoles emitting with a free-space wavelength of λ = 528 nm in a medium of index n = 1.33 (representative of the growth solution), separated by a distance of two wavelengths along the horizontal, and with the E-field oscillation axis along the vertical (representative of scattering of a vertically polarized input). A parallel set of vertically oriented interference fringes was observed between the dipoles, analogous to the ridge and trench nanotexture that was generated experimentally with inorganic phototropic growth using vertically polarized illumination (Figure 1b). Analagous simulations with dipoles separated by a series of

arbitrary distances exhibited similar fringes with the same pitch (Figure S5). This interference is hypothesized to promote the growth of the observed ordered nanotextures by producing a spatially varying, periodic near-field light intensity profile. Figure 5b presents a dipole simulation analogous to that in Figure 5a but representative of scattering of a horizontally polarized input in which the separation and oscillation axes were along the vertical and the horizontal, respectively. Analogous interference fringes were observed, but oriented horizontally, analogous to the orientation of the nanotexture observed experimentally when horizontally polarized illumination was used (Figure 1c).

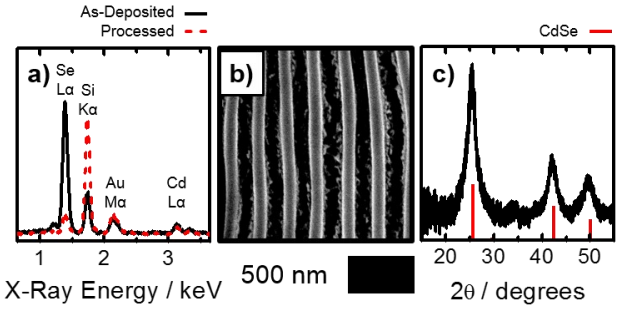

Figure 6. (a) Representative EDX spectra acquired from a film grown with vertically polarized λ_{avg} = 528 nm illumination as-deposited and after chemical processing with $CS_{2(l)}$. Representative (b) SEM and (c) GIXRD pattern of a film grown with vertically polarized λ_{avg} = 528 nm illumination after chemical processing with $CS_{2(l)}$.

Figure 6a presents representative energy-dispersive X-ray (EDX) spectra acquired from films grown using vertically polarized λ_{avg} = 528 nm illumination. The solid black trace corresponds to the as-deposited material, and exhibits Se Lα and Cd Lα signals from the deposit as well as Si Kα and Au Mα signals from the substrate. Quantification of the EDX data indicated a Se:Cd atomic ratio of 6:1. The as-deposited sample was then chemically processed by immersion in $CS_{2(l)}$ under reflux at ~ 46° C, to dissolve the fivefold excess of Se and yield stoichiometric CdSe.[48, 49] The dashed red trace in Figure 6a corresponds to an EDX spectrum of a film after processing with $CS_{2(l)}$, with quantification indicating a 1:1 Se:Cd atomic ratio. Figure 6b presents a representative SEM of a chemically processed film that was initially grown using vertically polarized λ_{avg} = 528 nm illumination. After processing, an ordered mesoscale morphology consisting of a ridge and

trench nanotexture was observed with a reduced feature size and slightly increased period (227 ± 2 nm) relative to the as-deposited film resulting from the removal of excess Se mass. Figure 6c presents a grazing-incidence X-ray diffraction (GIXRD) pattern acquired from a processed film similar to that depicted in Figure 6b. The GIXRD pattern displayed characteristic reflections indicative of polycrystalline CdSe. Scherrer analysis of these reflections indicated an approximate mean crystallite size of 4 nm. Thus, inorganic phototropic growth coupled with a low-temperature solution processing step effected the generation of CdSe films with highly ordered mesoscale morphologies that can be tailored via manipulation of the characteristics of the illumination during growth.

Conclusions

In summary, inorganic phototropic growth of Se-Cd via an optically directed electrochemical method using an isotropic aqueous solution, conformal unstructured illumination, and no physical or chemical templating agents, resulted in the generation of films that exhibited highly ordered and precise three-dimensional mesoscale morphologies. Growth in the dark resulted in films with no observable ordered nanotexture whereas growth using linearly polarized illumination resulted in films exhibiting controllable, periodic and anisotropic ridge and trench nanotextures over macroscopic areas. The characteristics of the film morphology were controlled by the illumination, with the in-plane direction of the nanotexture anisotropy and periodicity set by the input E-field vector and with a morphological period that scaled with the input λ_{avg}. Modeling of the inorganic phototropic growth process based on full-wave electromagnetic simulations of the interfacial optical interactions closely reproduced the experimentally observed nanotextures, including quantitative agreement with the observed morphological periods, indicating that nanotexture development is a product of the light-matter interactions during growth. Additional modeling of

the interfacial light scattering also supported the hypothesis that the film characteristics were determined principally by optical processes. Solution-phase processing of the as-deposited Se-Cd films in $CS_{2(l)}$ was used to produce stoichiometric, polycrystalline CdSe films with ordered, anisotropic nanotextures and controlled three-dimensional morphologies, demonstrating a scalable, high-throughput technique to prepare structured CdSe films over macroscale areas. The cumulative data suggest that inorganic phototropic growth may be extendable to generate precise mesostructures in a range of semiconducting materials, including constituents of the II-VI family of materials. Furthermore, the feature sizes, anisotropies, and pattern fidelities, as well as the macroscale conformality, of the morphologies generated in this work by inorganic phototropic growth resemble numerous environmentally facing biological interfaces with evolutionarily defined physical purposes. For example, butterfly wings exhibit nanoscale lamellar structures that produce defined structural coloration which provides superior visibility relative to pigmentary coloration, as well as possessing characteristics such as superhydrophobicity that enable anisotropic dewetting.[50, 51] Inorganic phototropic growth may thus provide a route towards the scalable, bottom-up generation of biomimetic materials with unique and potentially useful physical properties derived from complex but controllable mesoscopic interfacial structure.

Conflicts of Interest

There are no conflicts of interest to declare.

Acknowledgements

This work was supported by the "Light-Material Interactions in Energy Conversion" Energy Frontier Research Center funded by the U.S. Department of Energy, Office of Science, Office of Basic Energy Sciences under Award Number DE-SC0001293 and was also supported by the National Science Foundation, Directorate for Mathematical & Physical Sciences, Division

of Materials Research under Award Number DMR 1905963. The authors gratefully acknowledge R. Gerhart for assistance with photoelectrochemical cell fabrication and W.-H. Cheng and M. Richter for assistance with computer simulations. KRH, AIC, and MCM acknowledge graduate research fellowships from the National Science Foundation. MCM also acknowledges the Resnick Sustainability Institute at Caltech for fellowship support.

References

1. P. Vukusic and J. R. Sambles, *Nature*, 2003, **424**, 852-855.
2. C. Neinhuis and W. Barthlott, *Ann. Bot.*, 1997, **79**, 667-677.
3. S. Jeong, E. C. Garnett, S. Wang, Z. Yu, S. Fan, M. L. Brongersma, M. D. McGehee and Y. Cui, *Nano Lett.*, 2012, **12**, 2971-2976.
4. K. C. Park, H. J. Choi, C. H. Chang, R. E. Cohen, G. H. McKinley and G. Barbastathis, *ACS Nano*, 2012, **6**, 3789-3799.
5. D. Xia, L. M. Johnson and G. P. Lopez, *Adv. Mater.*, 2012, **24**, 1287-1302.
6. G. M. Wallraff and W. D. Hinsberg, *Chem. Rev.*, 1999, **99**, 1801-1821.
7. H. W. Choi, D. F. Farson, J. Bovatsek, A. Arai and D. Ashkenasi, *Appl. Opt.*, 2007, **46**, 5792-5799.
8. T. F. Deutsch, D. J. Ehrlich and R. M. Osgood, *Appl. Phys. Lett.*, 1979, **35**, 175-177.
9. A. E. Attard and D. E. Brown, *Appl. Opt.*, 1968, **7**, 511-516.
10. R. H. Micheels, A. D. Darrow and R. D. Rauh, *Appl. Phys. Lett.*, 1981, **39**, 418-420.
11. V. V. Doan and M. J. Sailor, *Science*, 1992, **256**, 1791-1792.
12. D. S. Barth, C. Gladden, A. Salandrino, K. O'Brien, Z. Ye, M. Mrejen, Y. Wang and X. Zhang, *Adv. Mater.*, 2015, **27**, 6131-6136.
13. M. R. Langille, M. L. Personick and C. A. Mirkin, *Angew. Chem. Int. Ed.*, 2013, **52**, 13910-13940.
14. M. Grzelczak and L. M. Liz-Marzán, *Chem. Soc. Rev.*, 2014, **43**, 2089-2097.
15. K. Ichimura, *Chem. Rev.*, 2000, **100**, 1847-1873.
16. M. Dasog, A. I. Carim, S. Yalamanchili, H. A. Atwater and N. S. Lewis, *Nano Lett.*, 2016, **16**, 5015-5021.
17. A. Paul, B. Kenens, J. Hofkens and H. Uji-i, *Langmuir*, 2012, **28**, 8920-8925.
18. J. Plain, G. P. Wiederrecht, S. K. Gray, P. Royer and R. Bachelot, *J. Phys. Chem. Lett.*, 2013, **4**, 2124-2132.
19. H. Ishitobi, I. Nakamura, T.-a. Kobayashi, N. Hayazawa, Z. Sekkat, S. Kawata and Y. Inouye, *ACS Photonics*, 2014, **1**, 190-197.
20. C. Fankhauser and J. Chory, *Annu. Rev. Cell Dev. Biol.*, 1997, **13**, 203-229.
21. J. M. Christie and A. S. Murphy, *Am. J. Bot.*, 2013, **100**, 35-46.
22. P. B. Tomlinson, *The Structural Biology of Palms*, Oxford University Press, New York, 1990.
23. A. Iwase, K. Sakai, A. Suzuki and R. van Woesik, *Estuar. Coast. Shelf Sci.*, 2008, **77**, 672-678.
24. M. C. Meier, W.-H. Cheng, H. A. Atwater, N. S. Lewis and A. I. Carim, *J. Am. Chem. Soc.*, 2019, **141**, 18658-18661.
25. A. I. Carim, N. A. Batara, A. Premkumar, H. A. Atwater and N. S. Lewis, *Nano Lett.*, 2015, **15**, 7071-7076.
26. A. I. Carim, N. A. Batara, A. Premkumar, R. May, H. A. Atwater and N. S. Lewis, *Nano Lett.*, 2016, **16**, 2963-2968.
27. A. I. Carim, K. R. Hamann, N. A. Batara, J. R. Thompson, H. A. Atwater and N. S. Lewis, *J. Am. Chem. Soc.*, 2018, **140**, 6536-6539.
28. X. Peng, L. Manna, W. Yang, J. Wickham, E. Scher, A. Kadavanich and A. P. Alivisatos, *Nature*, 2000, **404**, 59-61.
29. C. B. Murray, C. R. Kagan and M. G. Bawendi, *Annu. Rev. Mater. Sci.*, 2000, **30**, 545-610.

30. Y. Yin and A. P. Alivisatos, *Nature*, 2005, **437**, 664-670.
31. J. J. Storhoff, R. C. Mucic and C. A. Mirkin, *J. Cluster Sci.*, 1997, **8**, 179-216.
32. Y. A. Vlasov, N. Yao and D. J. Norris, *Adv. Mater.*, 1999, **11**, 165-169.
33. Y. Lin, A. Böker, J. He, K. Sill, H. Xiang, C. Abetz, X. Li, J. Wang, T. Emrick, S. Long, Q. Wang, A. Balazs and T. P. Russell, *Nature*, 2005, **434**, 55-59.
34. D. Xu, X. Shi, G. Guo, L. Gui and Y. Tang, *J. Phys. Chem. B*, 2000, **104**, 5061-5063.
35. M. Schierhorn, S. Boettcher, S. Kraemer, G. D. Stucky and M. Moskovits, *Nano Lett.*, 2009, **9**, 3262-3267.
36. J. S. Lee, M. V. Kovalenko, J. Huang, D. S. Chung and D. V. Talapin, *Nat. Nanotechnol.*, 2011, **6**, 348-352.
37. R. M. Penner, *J. Phys. Chem. C*, 2014, **118**, 17179-17192.
38. W. U. Huynh, J. J. Dittmer and A. P. Alivisatos, *Science*, 2002, **295**, 2425-2427.
39. M. Tomkiewicz, I. Ling and W. S. Parsons, *J. Electrochem. Soc.*, 1982, **129**, 2016-2022.
40. V. L. Colvin, M. C. Schiamp and A. P. Alivisatos, *Nature*, 1994, **370**, 354-357.
41. W. Xing, W. Yan, T. Ayvazian, Y. Wang, E. O. Potma and R. M. Penner, *Chem. Mater.*, 2013, **25**, 623-631.
42. S. Kinoshita and S. Yoshioka, *ChemPhysChem*, 2005, **6**, 1442-1459.
43. T. Sun, L. Feng, X. Gao and L. Jiang, *Acc. Chem. Res.*, 2005, **38**, 644-652.
44. J. W. Choi, M. Kim, N. S. Safron, M. S. Arnold and P. Gopalan, *ACS Appl. Mater. Interfaces*, 2014, **6**, 9442-9448.
45. G. F. Schneider, V. E. Calado, H. Zandbergen, L. M. Vandersypen and C. Dekker, *Nano Lett.*, 2010, **10**, 1912-1916.
46. J. N. Murphy, K. D. Harris and J. M. Buriak, *PLoS One*, 2015, **10**, e0133088.
47. X. Zhang, K. D. Harris, N. L. Y. Wu, J. N. Murphy and J. M. Buriak, *ACS Nano*, 2010, **4**, 7021-7029.
48. A. P. Saunders, *J. Phys. Chem.*, 1900, **4**, 423-513.
49. J. W. Moody and R. C. Himes, *Mat. Res. Bull.*, 1967, **2**, 523-530.
50. P. Vukusic, J. R. Sambles and C. R. Lawrence, *Nature*, 2000, **404**, 457.
51. Y. Zheng, X. Gao and L. Jiang, *Soft Matter*, 2007, **3**, 178-182.